Detection of Extragalactic Magnetic Fields through analysis of Photon Arrival Directions

by

Omkar H. Ramachandran

Thesis Advisor: Dr. Axel Brandenburg

Physics Department Reader: Dr. Dmitri Uzdensky

External Reader: Dr. Phil Armitage

Honors Council Reprasentative: Dr. John Cumalat

A thesis submitted to the

Honors Council of the

University of Colorado in partial fulfillment

of the requirements for

graduation with Latin honors for the degree of

Bachelor of Arts

Department of Physics

2018

This thesis entitled:
Detection of Extragalactic Magnetic Fields through analysis of Photon Arrival Directions
written by Omkar H. Ramachandran
has been approved for the Department of Physics

_____

Dr. Axel Brandenburg

_____

Dr. Dmitri Uzdensky

_____

Dr. Phil Armitage

_____

Dr. John Cumalat

Date _____

The final copy of this thesis has been examined by the signatories, and we find that both the content and the form meet acceptable presentation standards of scholarly work in the above mentioned discipline.

Ramachandran, Omkar H. (B.A., Physics)

Detection of Extragalactic Magnetic Fields through analysis of Photon Arrival Directions

Thesis directed by Dr. Axel Brandenburg

The existence of large-scale extragalactic magnetic fields (EGMFs) has been a subject of some debate over the last few decades. Recent work done on the analysis of cascade photons from high energy sources like Blazars (Tashiro and Vachaspati, 2013; Chen et al., 2015; Tashiro and Vachaspati, 2015) offer an exciting possibility of definitively proving the existence of such fields. In this thesis, the existing analysis of magnetic field measurements via cascade photon correlators will be extended to the most recent repository of data from the Fermi Large Area Telescope. In addition, a new Monte-Carlo routine to account for noise from the galactic disk will be discussed. Should this routine prove to be reliable, it could potentially be a means of explaining the anomalous observation of hemispheric dependence in the current literature.

Dedication

To friends and family

Acknowledgements

I would like to thank my advisor Dr. Axel Brandenburg for granting me a copious amount of much needed guidance and for providing me with the opportunity of contributing to cutting edge theoretical astrophysics in a meaningful way. I would also like to thank my parents for being the best mentors both personally and academically that any human being could ever hope for. I would like to thank the Laboratory for Atmospheric and Space Physics for providing me with an extremely comfortable and intellectually stimulating work environment. I would like to thank Dr. Tanmay Vachaspati for his valuable comments, which greatly enhanced the direction and progress of the project. Financial support was provided by the NSF Astrophysics and Astronomy Grant Program through the collaborative research grant AST-1615100 of Axel Brandenburg and Tina Kahniashvili. And finally, this work utilized the RMACC Summit supercomputer, which is supported by the National Science Foundation (awards ACI-1532235 and ACI-1532236), the University of Colorado Boulder, and Colorado State University. The Summit supercomputer is a joint effort of the University of Colorado Boulder and Colorado State University.

Contents

Chapter

Tables

Table

Figures

Figure

Chapter 1

Introduction

Gamma-rays from highly energetic astrophysical objects, such as TeV Blazars, have the interesting property of being able to probe any intervening magnetic field in their trajectory (Dolag et al., 2009; Neronov and Semikoz, 2009). Photons from such sources scatter off extragalactic background light (EBL) and produce highly energetic electron-positron pairs (Aharonian et al., 2006). These particles then Inverse Compton (IC) scatter off Cosmic Microwave Background (CMB) photons and in the process, generate a cascade of GeV Photons. These photons are suspected to carry information about the trajectory of the particles that IC scattered across them, leading to the possibility of inferring information about the particles by analysing the spatial arrangement of the GeV Photons. Specifically, if the electron-positron pair are deflected by an intervening magnetic field, then the cascade GeV Photons may carry information about the helicity of the field (Kahniashvili and Vachaspati, 2006).

The existence of an Extragalactic Magnetic Field (EGMF) is a crucial component in the current models of intergalactic magnetic field formation (Neronov and Semikoz, 2009; Ryu et al., 2008), primarily as candidate seed fields (Kronberg et al., 2008b; Bernet et al., 2008; Clarke et al., 2001). Consequently, a lot of effort has been put into understanding the theoretical origins of an EGMF, and – since the advent of large scale, high precision Gamma Ray telescopes like the Fermi Large Area Telescope (LAT) – on detecting their presence.

Several existing theoretical frameworks for the origins of an EGMF tend to place it at significant events in the early universe, such as during the electroweak phase transition (Vachaspati

and Vilenkin, 1991; Vachaspati, 2001). This particular scenario also makes the prediction that the helicity of the field is left-handed (Vachaspati, 2001).

1.1 Detection of EGMF through photon spatial distribution

The method of reconstructing properties of the magnetic field from observations of GeV cascade photons involve the analysis of correlators functions of GeV photon position that directly relate to either the normal, longitudnal or helical components of a magnetic field (Tashiro and Vachaspati, 2013).

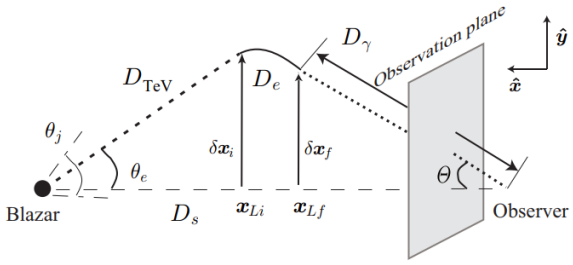

Figure 1.1: Schematic showing the mechanism through which electron-positron pairs formed through the scattering of a TeV gamma ray and an EBL photon capture information about the intervening magnetic field. Figure taken from (Tashiro and Vachaspati, 2013).

TeV photons from very distant sources cannot travel freely in space, due to potential interaction with the EBL, causing pair production. The mean free path of such a photon with energy $E_{\rm TeV}$ is given by(Neronov and Semikoz, 2009):

$$D_{\rm TeV}(E_{\rm TeV}) \sim 80 \frac{\kappa}{(1+z_s)^2} \left(\frac{E_{\rm TeV}}{10\ \rm TeV} \right)^{-1} \ \rm Mpc. \tag{1.1}$$

Similarly, the produced electron and positron are also liable to inverse compton scatter with photons from other sources. The most abundant of these are Cosmic Microwave Background (CMB) photons. It is possible, once again, to define a mean free path as follows:

$$D_e \sim 30(1-z_e)^{-4} \left(\frac{E_{\rm TeV}}{10\ \rm TeV} \right)^{-1} \ \rm kpc. \tag{1.2}$$

Using these parameters, and perturbing the momemtum of the pair-produced particle by a Lorentz impulse, the deviation angle for the resulting cascade photon can be shown to be (Tashiro and Vachaspati, 2013, 2015):

$$\Theta(E_\gamma) \simeq 7.3 \times 10^{-5} \frac{B}{10^{-16}\ G} \left(\frac{E_\gamma}{100\ \text{GeV}}\right)^{-3/2} \left(\frac{D_s}{1000\ \text{Mpc}}\right)^{-1}. \tag{1.3}$$

If we now consider a normalized version of this deflection angle, say $\hat{\Theta}$, so as to remove any dependence to unknowns like the distance to the source D_s, it is possible to show that the correlator

$$G(E_1, E_2) = \langle(\hat{\Theta}_1 \times \hat{\Theta}_2) \cdot \hat{D}_s\rangle \tag{1.4}$$

relates to the helical component of the intervening field M_H (Tashiro and Vachaspati, 2013):

$$G(E_1, E_2) \sim \frac{1}{2} M_H(|r_{12}|) r_{12}, \tag{1.5}$$

where r_{12} reprasents the vector $D_{\text{TeV}}(E_1) - D_{\text{TeV}}(E_2)$.

1.2 Measuring $G(E_1, E_2)$

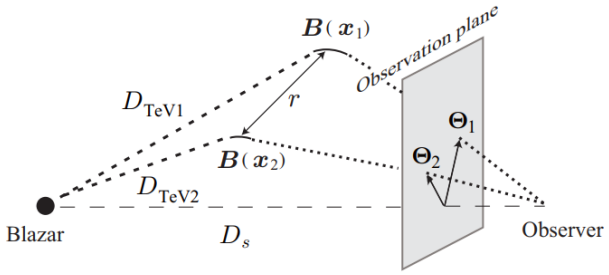

Figure 1.2: Deviation of two photons released at slightly different angles from the original high energy source due to influence from the intervening magnetic field. Figure taken from (Tashiro and Vachaspati, 2013).

Looking at Figure 1.2 and Equation 1.5, we can reconstruct the correlator G as follows:

$$G(E_1, E_2) = \langle(\Theta_1 \times \Theta_2) \cdot \hat{D}_s\rangle. \tag{1.6}$$

However, it isn't possible to know D_s precisely because every photon from a sufficiently distant high energy source will deviate a certain amount if passing through an intervening magnetic field. However, looking at equation (1.3), it is clear that the deflection angle varies inversely with E_γ. Thus, we can choose a sufficiently high energy photon and approximate it as $\hat{D}_s$. Applying this modification to G leads to the following:

$$G(E_1, E_2; E_3) = \langle (\Theta(E_1) - \Theta(E_3)) \times (\Theta(E_2) - \Theta(E_3)) \cdot \Theta(E_3) \rangle. \tag{1.7}$$

Normalizing (1.7) gives us the following new statistic Q, defined as follows:

$$Q(E_1, E_2, E_3) = \langle (\hat{\boldsymbol{n}}(E_1) \times \hat{\boldsymbol{n}}(E_2)) \cdot \hat{\boldsymbol{n}}(E_3) \rangle \quad \text{for} \quad E_1 < E_2 < E_3. \tag{1.8}$$

It is important to note here that Q is a function that will correlate with the helical component of the intervening magnetic field iff the measurement is done for photons originating from the same source. When physically measuring the statistic from diffuse gamma ray data, it is impossible to correlate cascade photon to source – in fact, it isn't even possible to independantly determine if a photon was generated through a cascade! The simplest way to work around this problem is to design a window function that allows for the measurement of Q over a range of resolutions and to actively avoid any known source of high energy photons in the sky. As a result, the measurement of Q is done over patches of a prescribed radius around each photon in the highest energy bin E_3. Mathematically, this changes equation (1.8) to the following:

$$Q(E_1, E_2, E_3, R) = \frac{1}{N_3} \sum_{k=1}^{N_3} (\hat{\boldsymbol{\eta}}_1 \times \hat{\boldsymbol{\eta}}_2) \cdot \hat{\boldsymbol{\eta}}_k(E_3), \tag{1.9}$$

where $\hat{\boldsymbol{\eta}}_i = \frac{1}{N_i} \sum_{i \in D(\hat{\boldsymbol{n}}_k, R)} \hat{\boldsymbol{n}}_i(E_a)$ and $D(\hat{\boldsymbol{n}}, R)$ defines a patch of radius R around a photon $\hat{\boldsymbol{n}}$. For the actual computation of Q, (Tashiro and Vachaspati, 2013) binned the photons observed by the Fermi LAT into one of five equally spaced energy bins between 10 and 60 GeV. At each run of the analysis pipeline, three of these bins were chosen and every possible triple involving exactly one photon from each bin was computed and averaged. There have been further updates to this workflow, specifically by (Chen et al., 2015), but the basic method remains largely the same.

1.3 Dynamics of Q in environments containing source and background

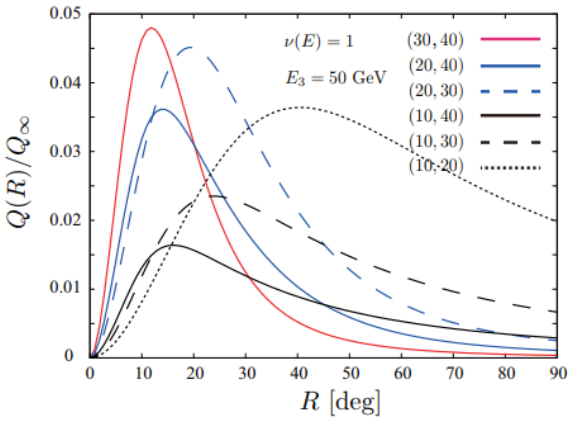

Figure 1.3: Plot of $Q(R)$ vs the correlator measured for a single source Q_∞ for $E_3 = 50$ GeV with $B = 2 \times 10^{-13}$ G and $D_s = 1$ Gpc. Figure taken from (Tashiro and Vachaspati, 2015).

As mentioned in the previous section, it isn't really ideal to use a correlator that assumes computation over photons originating from the same source. To account for this, a detailed theoretical analysis of the effect of background photons that needn't necessarily originate as cascade photons from a TeV source was performed by (Tashiro and Vachaspati, 2015). Some of the major results of that study were as follows:

- Peaks for curves that share an E_2 bin occur at roughly the same patch radius R. In addition, performing the computation over the combination $(30-40, 40-50, 50-60)$ GeV is supposed to yield the largest peak at the smallest patch radius.

- The study came up with a very simple formula to predict the peak of a $Q(R)$ curve given $Q(R)$ for a different value of the intermediate energy bin E_2:

$$R_{\text{peak}}(E_2) \simeq R_{\text{peak},0} \left(\frac{E_2^{(0)}}{E_2} \right)^{3/2}, \tag{1.10}$$

  where $R_{\text{peak},0}$ is the location of the peak for the known curve with intermediate energy $E_2^{(0)}$

All of the predictions discussed in this section will be analysed in detail in Chapter 2

Chapter 2

Preparation and Analysis of Fermi Data

2.1 Outline of Filtering method

The predictions made in (Tashiro et al., 2014) – and later in (Chen et al., 2015) – assumed that the photons involved in computing Q originated purely from extragalactic sources. Going back to the mean free path of TeV photons defined in (Tashiro and Vachaspati, 2013), but defining it in terms of cascade photon energy instead of TeV photon energy gives us the following:

$$D_{\rm TeV} \propto 80 \left(\frac{E_{\rm TeV}}{10\,{\rm TeV}} \right)^{-1} \ {\rm Mpc}$$

$$\implies D_{\rm TeV} \sim 80 \left(\frac{E_\gamma}{88\ {\rm GeV}} \right)^{-1/2} \ {\rm Mpc}. \tag{2.1}$$

In essence, an up-scattered photon with $E \sim 50$ GeV likely originated from a source that traveled an average of 80 Mpc before the scattering event. As a result, we can already identify a major source of noise in the high energy photons originating from the galactic disk. Similarly, photons originating from scattering events in the upper atmosphere also have to be filtered for. In all, the raw data obtained from the Fermi LAT was filtered using the following constraints – mostly following the procedure used in (Tashiro et al., 2014) and later (Chen et al., 2015):

- For measuring Q, I used 404 weeks of data from Pass 8 of the Fermi LAT, specifically, from weeks 100 through 504 (previous studies involving cascade photon analysis has only used the older Pass 7 repository).

- To avoid contamination from the galactic disk, the photons in the highest energy bin were constrained to the region on the sky described by $|b| > 70°$. The condition was later tightened to $|b| > 80°$, further increasing the likelihood that the photons used in the analysis were free from galactic contamination. The results presented in this document only report measurements done with $|b| > 80°$. This is due to my findings when running Monte-Carlo simulations including corrections for the galactic disk seemingly indicating that $|b| > 70°$ already includes too much contamination from the galactic disk to yield any significant measurement of $Q(R)$

- To avoid contamination from cosmic ray scattering in the upper atmosphere, photons arriving at zenith angles greater than 100° were discarded.

- Finally, the selected data with these characteristics was filtered so as to only use photons that were marked as 'CLEAN' or 'ULTRACLEAN' using the `gtmktime` command in the Fermi `sciencetools` package. (Chen et al., 2015) tightened the constraint to only use 'ULTRACLEAN' photons, but our early analysis suggested that there was very little difference in the signal – this was also observed by (Chen et al., 2015) –, and thus photons marked both as CLEAN and ULTRACLEAN were used to increase the overall observed flux of high energy photons.

- The spacecraft's rocking angle at the time of event detection was also constrained to be less than 52°.

2.2 Computing Q from filtered data

As discussed in Section 1.2, the pseudo-scalar of interest is the following:

$$Q(R, E_1, E_2, E_3) = \frac{1}{N_3} \sum_{k=1}^{N_3} \hat{\boldsymbol{\eta}}_1 \times \hat{\boldsymbol{\eta}}_2 \cdot \hat{\boldsymbol{\eta}}_k(E_3), \tag{2.2}$$

where $\hat{\boldsymbol{\eta}}_a = (1/N_a) \sum_{i \in D(\hat{\boldsymbol{n}}_k, R)} \hat{\boldsymbol{n}}_i(E_a)$, $a = 1, 2$ and $D(\hat{\boldsymbol{n}}, R)$ implies that only photons in the E_1 and E_2 bin that lie within a patch of radius R around any given E_3 photon are to be used in the

computation. Of course, the fastest way to do this computation is to perform the summation first for each of the three vector sets and then do one triple product for the resulting sums. This reduces the overall complexity of the routine from $O(N^3)$ to $O(N)$. For each $Q(R)$ computed, the standard errors were defined as follows:

$$\sigma_Q(R) = \frac{\sigma(Q(R, E_3))}{\sqrt{N_3}}, \tag{2.3}$$

In essence, the error is simply the standard deviation of triple products for a patch of a given radius around a photon in E_3, normalized by the number of photons in E_3 within the patch. The normalization factor is added in to account for the fact that there may be a different number of E_3 photons in different patches in the sky. There is one major issue with this approach: Computing the standard error as in equation (2.3) assumes that $Q(R = R_j)$ is independent of $Q(R \neq R_j)$, which isn't true. Computing $Q(R = 4^\circ)$, for instance, will necessarily contain every triple product in $Q(R < 4^\circ)$. Therefore, while I present plots with error-bars defined by $\sigma_Q(R)$, statistical significance will always be determined by comparing the distance from 0 in steps of σ_M, the standard deviation of the Monte-Carlo without corrections for the galactic disk.

2.3 Description of the Analysis Workflow

Once the Fermi Data has been filtered in accordance to the constraints detailed in the previous section, the $Q(R)$ curve was determined as follows:

- Starting with the filtered data, I first masked out photons in a 2° radius around known high energy sources from 1FHL catalog. The reason for doing this is fairly simple: The theory behind this analysis routine is designed specifically for diffuse emissions. If one were to look at a patch of sky with a known high energy source, our $Q(R)$ curve will, for that patch, will be dominated by a single source, potentially contaminating the $Q(R)$ signal.

- Once this is done, I added Gaussian noise to the data consistent with the Point Spread Function (PSF) – or the resolution error – of the Fermi telescope. [1] This step is arguably

[1] https://fermi.gsfc.nasa.gov/ssc/data/analysis/documentation/Cicerone/Cicerone_LAT_IRFs/IRF_PSF.html

not critical, since the resolution errors were observed to be in the vicinity of 10 arcminutes, which corresponds roughly to 10% of σ_Q. As I will soon demonstrate, the error bars on the Monte-Carlo control curve are much larger, thus negating the significance of accounting for uncertainties in the resolution.

- Once this was done, I evaluated the triple product, along with the standard error for $Q(R)$, $Q_{\,\mathrm{north}}(R)$ and $Q_{\,\mathrm{south}}(R)$ at 30 equally spaced points on $R \in [0°, 25°]$.

- In the interest of speed, my Python scripts were vectorized whenever feasible, and the triple product sum was evaluated sum-first to reduce the routine to a manageable complexity.

- The program was eventually parallelized using `mpi4py`, a Python package that allows for the use of the Message Passing Interface (MPI) in direct Python code. However, this modification proved to be more consequential in the Monte-Carlo analysis, given the more expensive nature of the computation – eventually, I had to write the routine in Nvidia's CUDA platform to allow for evaluation on a GPU – initially my personal GeForce GTX 760 and later on the CU supercomputer's GPU nodes, which were Nvidia Tesla K80s (Anderson et al., 2017).

2.4 Results

This section will report the results of applying the analysis workflow described in the previous section. The analysis here will simply confirm – or attempt to confirm – trends in Q that we would expect, given the theoretical framework described in Section 1.3 and comparison with synthetic control curves obtained through the Monte-Carlo routine described in Chapter 3.2.

2.4.1 A word on notation

In the remainder of this document, I will use the following shorthand for describing specific energy bin combinations: The triple (x, y, z) refers to the combination of bins given by $E_1 \in$

(E_1, E_2)	$(10, 20)$	$(10, 30)$	$(20, 30)$	$(10, 40)$	$(20, 40)$	$(30, 40)$
R_{peak}	None	$14.1°$	$11.8°$	$9.7°$	$13.3°$	$14.0°$

Table 2.1: Location of R_{peak} for different energy bin combinations

$[x, x + 10]$ GeV, $E_2 \in [y, y + 10]$ GeV, $E_3 \in [z, z + 10]$ GeV. For example, the triple $(30, 40, 50)$ signifies that $E_1 \in [30, 40]$ GeV, $E_2 \in [40, 50]$ GeV, $E_3 \in [50, 60]$ GeV.

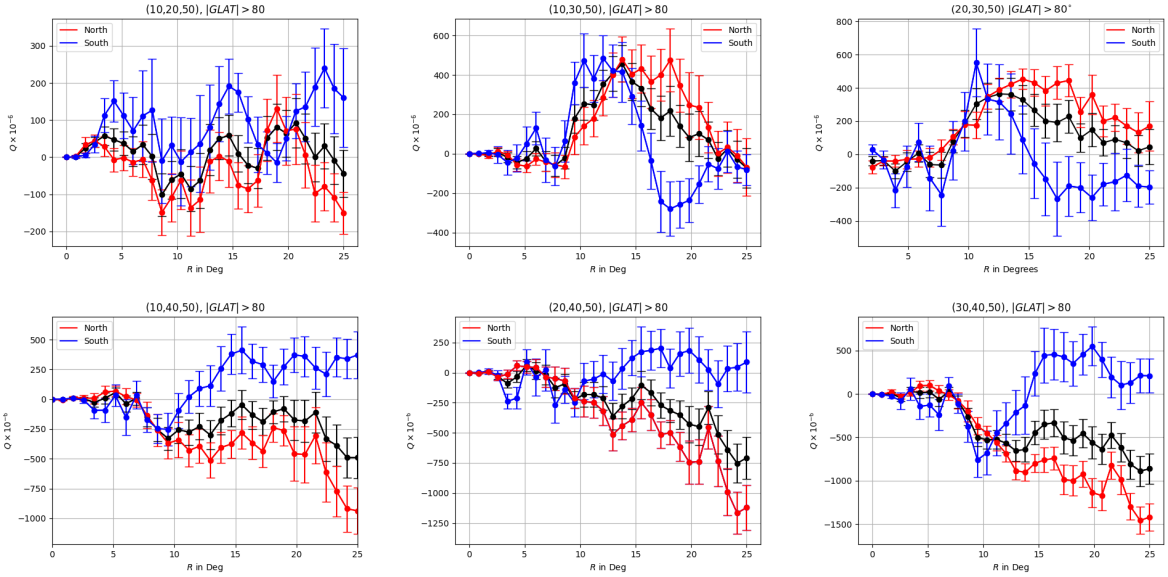

Figure 2.1: Plots of Q vs the patch radius R around each E_3 for every possible bin combination between 10 and 60 GeV

2.4.2 Similarity of $Q(R)$ for curves with the same E_2

As discussed in Section 1.3, the peaks in $Q(R)$ are expected to occur at the same patch radius for triples that share the same intermediate value bin (Tashiro and Vachaspati, 2015). This is very clearly seen in Figure 2.1. We also observe that every peak, except for $(10, 20, 50)$ are prominent and clearly defined. This is a significant and positive difference from the earlier (Chen et al., 2015) study where certain energy bins were too scattered to discern prominent peaks. In addition, observe that curves that share their intermediate energy bins have the same overall structure, specifically

where their peaks, if they exists, are located. This is in direct agreement with (Tashiro and Vachaspati, 2015). In addition, the study predicted that the magnitude of the peaks for $(X, 40, 50)$ and $(X, 30, 50)$ increases with X, which is precisely what we see in Figure 2.1. The implications of this are rather profound: The fact that both the overall curve and curves computed over a given hemisphere share structure with every other energy combination with the same E_2, implies that should the hemispheric dependence be purely due to galactic interference, then proving this for one combination, say $(30, 40, 50)$ is sufficient to prove it for every other combination with $E_2 = 40$ GeV.

2.4.3 Comparison of $Q(R)$ vs Monte-Carlo (uncorrected for Galactic noise)

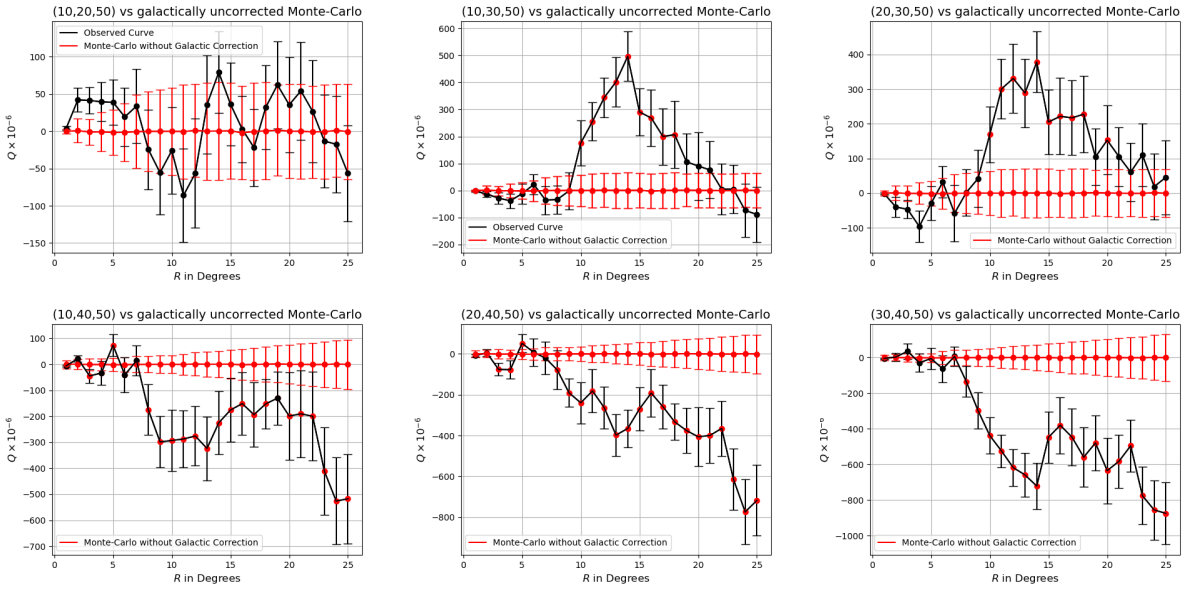

Figure 2.2: Observed data overlaid on Monte-Carlo generated error bars. Points that lie further than 2σ away from the mean of the simulated data are colored in red

When comparing each $Q(R)$ curve to its corresponding synthetic dataset generated via the procedure listed in Section 3.2 – the Monte-Carlo simulation accounts for differing time exposure but not for contamination from the galactic disk – we see that for almost every energy combination, there is a significant combination of data points that lie 2σ or higher beyond the mean of the synthetic

dataset, with some curves, like $(30, 40, 50)$ lying as far 7σ away at the peak at $R = 14°$, thus clearly demonstrating profound statistical significance. While this Monte-Carlo simulation does not take into account galactic contamination effects, it must be noted that for small R, these are insignificant. Each synthetic curve represents averages of 10^4 individual Monte-Carlo realizations.

2.4.4 Hemispheric Dependence

A significant difference between my results and the results of Tashiro et al. (2014) and Chen et al. (2015) is the observation of hemispheric deviation in every $Q(R)$ curve except for $(10, 20, 50)$. In this section, I will analyze this deviation in every family for curves, demarcated by E_2 as in the previous section, and attempt to provide an explanation for this observation.

2.4.4.1 $E_2 = 20$

We have exactly one combination with $E_2 = 20$. And, as established in Section 1.3 (Figure 1.3), the peak for $(10, 20, 50)$ lies at the largest R of all 6 combinations (approximately $40°$) (Tashiro and Vachaspati, 2015), thus adequately explaining the absence of any predominant signal. In addition to this, there is no real deviation between $Q_{\,\mathrm{north}}$ and $Q_{\,\mathrm{south}}$ for any R.

2.4.4.2 $E_2 = 30$

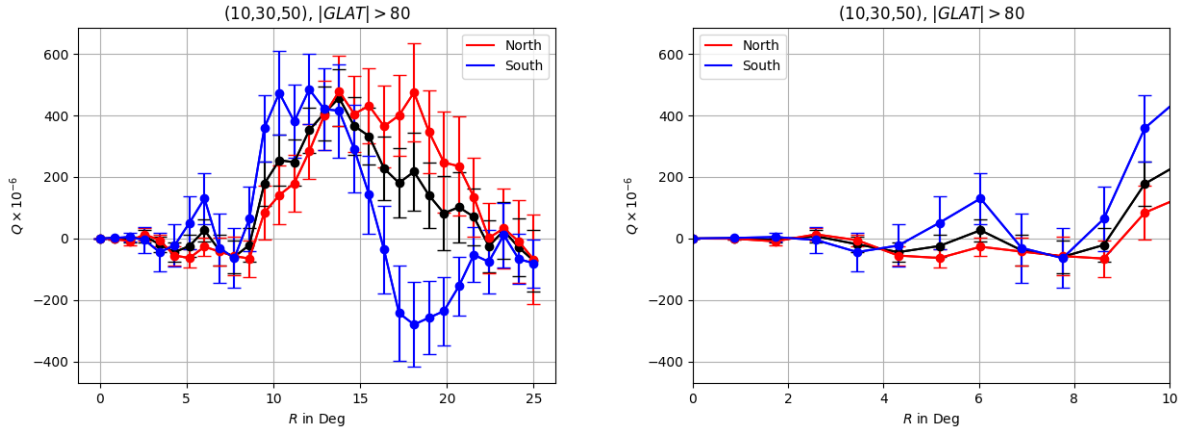

Figure 2.3: Plot of $Q(R)$ for $(10, 20, 50)$ for (a) $R \in [0°, 25°]$ and (b) $R \in [0°, 10°]$

When $E_2 = 30$, we see a more robust display of hemispheric deviation, particularly for $R \geq 15°$ (Figure 2.3). This will turn out to be a trend for the rest of the document wherein the curve splits itself neatly into two regimes: (1) Low R which is predominantly characterized by hemispheric coherence – i.e, Q_{north} and Q_{south} track each other – and (2) high R where we start seeing significant hemispheric deviation. I define hemispheric deviation as sections of Q where Q_{north} and Q_{south} deviate by more than $2\sigma_M$, where σ_M is the uncertainty of the (non galaxy corrected) Monte-Carlo. And, looking at Figure 2.1, we see that the $(20, 30, 40)$ curve also shows these two regimes demarcating slightly earlier, thus potentially demonstrating earlier peak formation consistent with (Tashiro and Vachaspati, 2015).

2.4.4.3 $E_2 = 40$

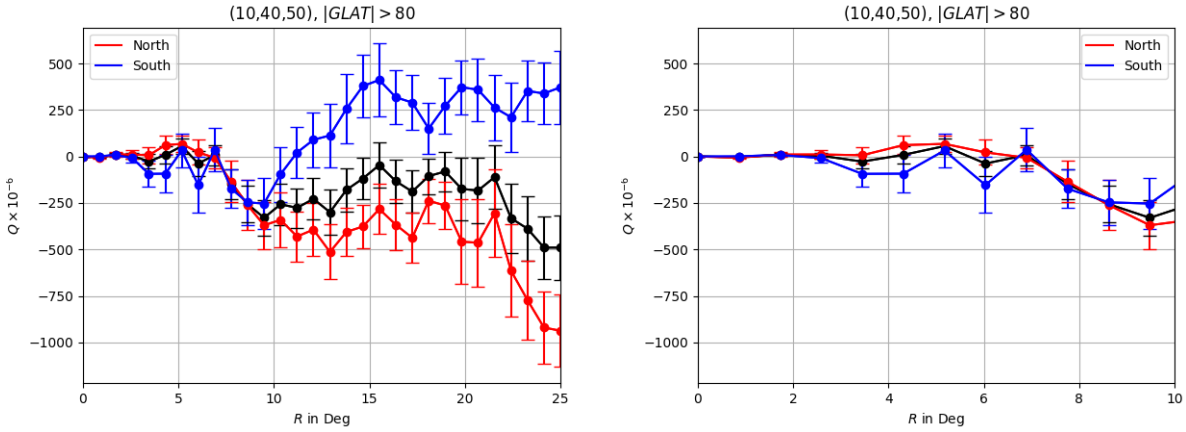

Figure 2.4: Plot of $Q(R)$ for $(10, 40, 50)$ for (a) $R \in [0°, 25°]$ and (b) $R \in [0°, 10°]$

$E_2 = 40$ is probably the best demonstration of the effect described in the previous section. Here, we find a clear separation of hemispheric coherence and hemispheric deviation at $R \sim 10°$. This pattern seems to persist in $(20, 40, 50)$ and $(30, 40, 50)$, with demarcations occurring slightly later for $E_1 = 20, 30$. This appears to be in conflict with Tashiro and Vachaspati (2015), which predicts the peak for $(30, 40, 50)$ to occur sooner than $(10, 40, 50)$ and $(20, 40, 50)$, but my present guess – which will be partially defended in Chapter 3 – is that this is due to relatively higher galactic interference in $(10, 40, 50)$ and $(20, 40, 50)$, thus causing the generation of false peaks in the region immediately after $R = 10°$.

2.5 Absence of Hemispheric Dependence in fully constrained datasets

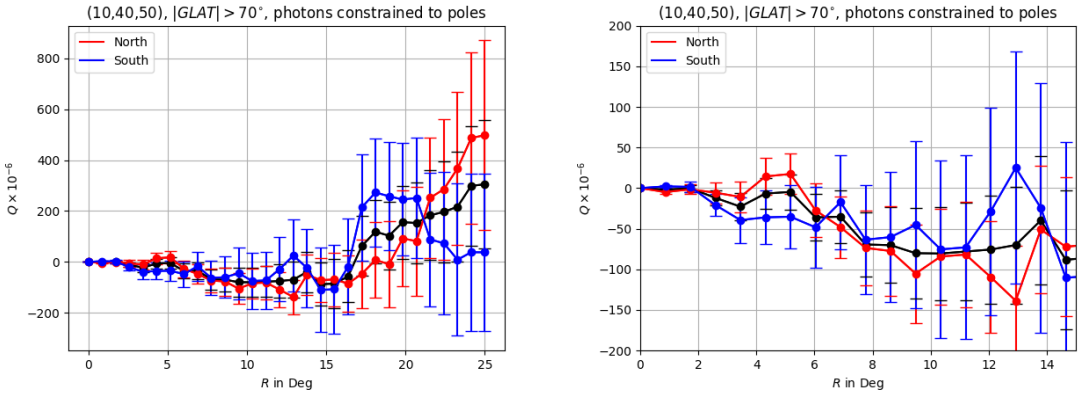

Figure 2.5: Plot of $Q(R)$ where photons in every bin is constrained to (left) $|GLAT| > 80°$ and (right) $|GLAT| > 70°$

A naive way of testing if hemispheric dependence is an inherent part of the signal can be achieved by simply constraining every electron to the poles (in this case, to $|GLAT| > 70°$). Looking at Figure 2.5, we notice that there is no demarcation between coherence and deviation. While this gives us very little to go on in terms of pinpointing a source, this simple experiment demonstrates that **hemispheric deviation is likely a result of contamination**.

Chapter 3

Description of the Monte-Carlo Simulation

Following the analysis done in the previous section, it was imperative that I write a Monte-Carlo simulation to account for the following:

- Since the standard error does not accurately represent the statistical significance of $Q(R)$, it is necessary to create a synthetic dataset that can act as a measurement control
- Given our observations of hemispheric dependence, particularly at high patch radius R, it is crucial to build a simulation that either recreates the effects of galactic interference, or provides a way to rule out extragalactic influence.

In this section, I will describe the method followed by the Monte-Carlo simulation, highlight areas where the assumptions used may not be completely accurate and elaborate on the reasons why these inaccuracies do not compromise the sanity of the overall simulation.

3.1 Overall Schematic

The basic schematic of the Monte-Carlo simulation is as shown in figure 3.1. The goal of the simulation, as described above is to account for the fact that the uncertainty in $Q(R)$ is not, in fact, $\sigma_Q R$. Having said that, if we were to generate a Monte-Carlo that accounts for every aspect of the Fermi LAT's measuring properties – save the presence of an extragalactic field – the error bars do begin to account for the actual uncertainty in the system as a result of the Central Limit Theorem.

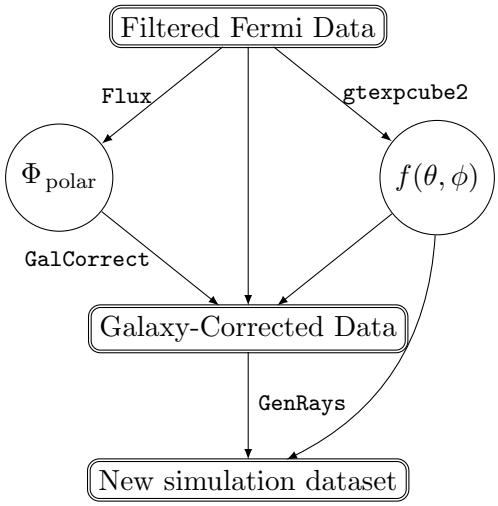

Figure 3.1: Overall Schematic followed by the Monte-Carlo. The labels above each arrow represents the exact routine in my workflow that completes aforementioned step

The main simulation is conducted through the following sequence of steps:

- Starting with Fermi data filtered using the constraints specified in Section 2.1, we need to compute two important pieces of information: (1) the joint probability density $f(\theta, \phi)$ of finding a photon at a given location (θ, ϕ) based on the amount of time the spacecraft looked at that point in the sky and (2) the flux $\Phi(\theta, \phi)$ of photons near the poles (the exact procedure involved in determining the dimensions of this spherical cap will be discussed in Section 3.5).

- Now, using this information, filter the data first by resampling photons corresponding to the flux Φ in accordance to $f(\theta, \phi)$. The cumulative effect of doing this will be to filter out, on average, any extragalactic contribution to the signal in the lower latitudes.

- Finally, run the analysis workflow used in Chapter 2 on this new semi-synthetic dataset to obtain a control curve for $Q(R)$ for different energy bin combinations.

3.2 Accounting for Exposure Time

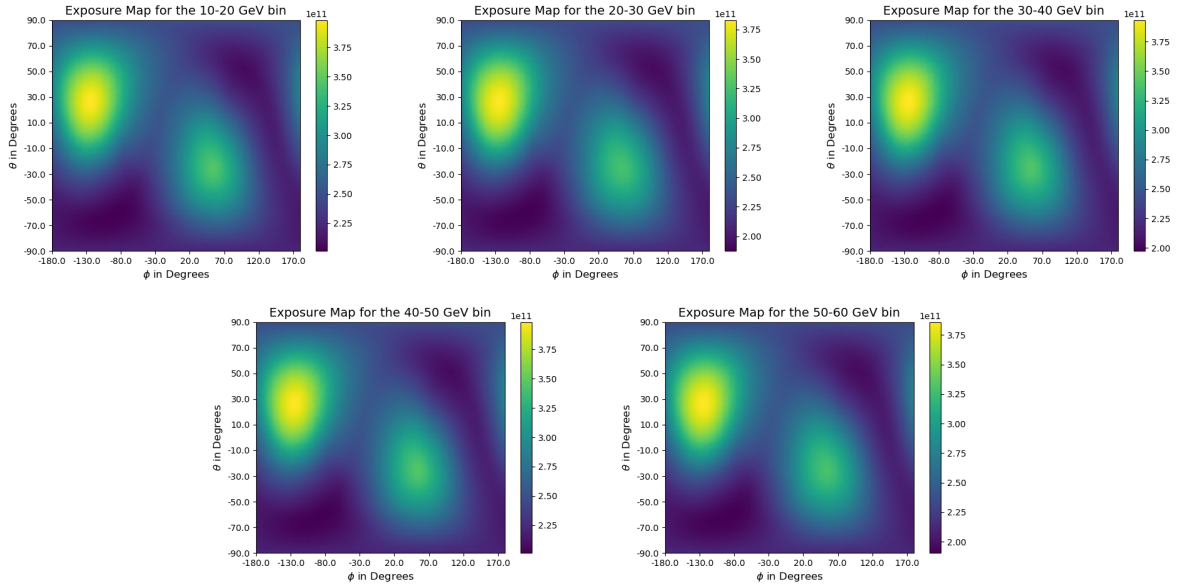

Figure 3.2: Exposure maps computed for photons in different energy bins. θ and ϕ here represent the b and l coordinates respectively. The color bar has units of seconds

The Fermi LAT's coverage of the sky is not uniform. As a result, writing the main Monte-Carlo routine is not as simple as generating rays with uniform $\cos\theta$ and ϕ on $[-1, 1]$ and $[0, 2\pi]$ respectively. Fortunately, the Fermi `sciencetools` [1] package has functions that can pull out exposure time for every point in the sky. Specifically, I used the `gtexpcube2` command to generate a exposure map for the photons in each energy bin. The resulting sky-maps are as shown in Figure 3.2. An interesting observation to make here is that the large bright patch in the southern hemisphere is lower in amplitude than the corresponding patch in the northern hemisphere. Indeed, when we compute the total time spent in each hemisphere, we find that the satellite spends roughly 10% less time in the South (8.01% to be exact). This would certainly explain the observed tendency for the $Q(R)$ curve to follow the $Q_{\text{north}}(R)$ for large R.

[1] Freely available here: https://fermi.gsfc.nasa.gov/ssc/data/analysis/software/

3.2.1 Computing Photon probability from exposure maps

In the absence of a cosmic magnetic field – and the galactic disk –, the probability of finding an electron at a given $(\theta,\ \phi)$ is directly related to the amount of time spent by the satellite at that pixel. The constant of proportionality in this case can be pinned down by utilizing the fact that the probabilities summed over every $(\theta,\ \phi)$ has to be equal to 1. Therefore, given an exposure function $T(\theta, \phi)$, the joint probability density $f(\theta, \phi)$ is simply

$$f(\theta, \phi) = \frac{T(\theta, \phi)}{\sum_{\theta,\phi} T(\theta, \phi)}. \tag{3.1}$$

Therefore, the position of incidence of a random photon on the sky can be computed from the $f(\theta, \phi)$ via the following procedure:

- Compute the marginal density along ϕ:

$$f_\phi(\phi = \phi_i) = \sum_\theta f(\theta, \phi_i). \tag{3.2}$$

- Choose a variate ϕ from f_ϕ. My initial Monte-Carlo simply used NumPy's `random.choice()` function, but I later wrote a rejection algorithm to speed up the simulation.

- Next, compute $f(\theta|\phi_i)$ from the marginal density:

$$f(\theta|\phi_i) = \frac{f(\theta, \phi_i)}{f_\phi(\phi_i)}. \tag{3.3}$$

- Using an appropriate sampling method generate θ_i from $f(\theta|\phi_i)$.

While this is one way of accounting for time exposure, it is possible to generate a Monte-Carlo routine simply by resampling the observed data Chen et al. (2015) in accordance to $f(\theta, \phi)$. In essence, if one were to start with the set of all photons in a given $Q(R)$ run and then scramble the locations of every photon in accordance to $f(\theta, \phi)$, then one should end up with a dataset with photons distributed as if through the procedure detailed above. This analysis has already been done (Chen et al., 2015) and it was determined that the error-bars are not significantly different from

the standard Monte-Carlo routine. As a result, I did not use this second method for the Monte-Carlo simulation involving only time exposure. However, I did end up using a similar technique to account for corrections to data in the galactic disk.

3.3 Accounting for contamination from the Galactic disk

The major problem with writing a Monte-Carlo routine that purely follows the procedure described in the previous section is that it doesn't account for the fact that the galactic disk is a major source of high-energy photons that will almost certainly interfere with the our predictions of $Q(R)$. Accounting for contamination from the Milky Way will allow for testing the hypothesis proposed in the previous chapter about the observed hemispheric dependence being influenced primarily by noise from the galactic disk.

There are two general ways of handling the galactic disk: (1) Add in a simulation of the galactic disk to the Monte-Carlo, which will almost certainly involve computationally expensive simulations using a software package like GALPROP[2] or (2) come up with a routine that will wipe out the signal if and only if the source is extragalactic – In other words, if the signal does not vanish under this proposed routine, then the source cannot be extragalactic and is thus most likely caused by the Milky Way.

3.4 Demonstrating galactic origin of hemispheric deviation

Consider the following experiment: Suppose the source of the hemispheric deviation was, in fact, from an extragalactic source, which due to some hitherto unknown interaction with the galactic disk, only shows up if we stretch our analysis to the lower latitudes. If this were the case, it should be possible to introduce noise to our dataset equivalent to the flux of photons from extragalactic sources (assuming this information is known) and over a large number of realizations, wipe out the deviations in Q_{north} and Q_{south}. If however, we perform this experiment and find that the signal for large R remains completely unchanged, then the deviating signal cannot be caused

[2] https://galprop.stanford.edu/

by an extragalactic source. Therefore, one would have to assume that the origin of this signal is, in fact, galactic. The same argument that ruled out an extragalactic source cannot work for a galactic source, since the flux of extragalactic photons is far smaller than photons originating in the galactic disk. In other words, for each triple that we eliminate through our added noise, there are many other triples that still contribute to a deviating signal.

3.5 Measuring extragalactic flux

The core assumption in constraining E_3 photons to the polar caps is to minimize the effect of galactic noise. In other words, for photons in each energy bin, there exists $b_p \geq 0$ such that photons within this region are completely devoid of galactic noise. Of course, in practice, one can never eliminate noise, but we can certainly define an acceptable threshold.

3.5.1 The vertical profile of $N(\theta, \phi)$ as a measure of galactic influence

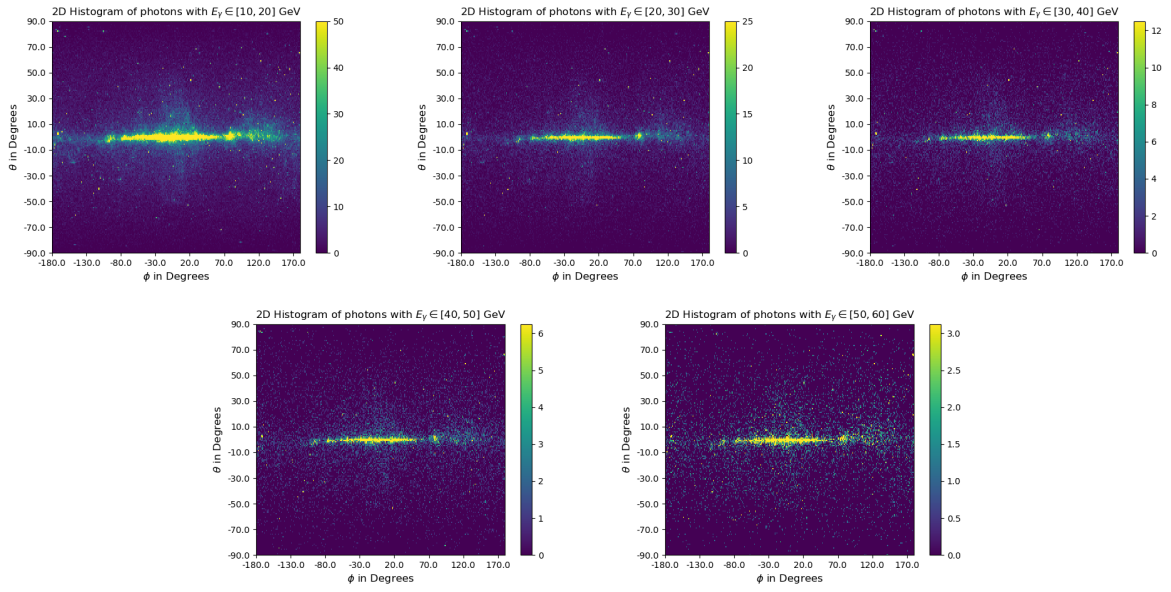

Figure 3.3: 2D Histogram representing the profile of photons of different energies in the sky. Note that the color bar for each panel has different maximal values and is in units of individual photon count at a given pixel

At this point, we need a good way of benchmarking the extent of the galactic disk for photons at different energies. One obvious way to do this is to simply look at the vertical profile of photons in different energy bins. Looking at any of the charts in Figure 3.3, but particularly at the more populated low energy bins, we see that there are two structural components to the galactic disk: a thin, but extremely bright central disk and a diffuse, but less bright vertical distribution (Porter et al., 2017; McMillan, 2017). If my guess – following our discussion in Chapter 2 – that the hemispheric deviation is caused by galactic noise is correct, then the region of hemispheric coherence must account for regions where the ratio between the flux of high-energy photons from the galaxy and the corresponding flux from extragalactic sources is low enough to sustain a statistically significant signal. Therefore, choosing R_p such that large scale hemispheric deviation was observed (i.e., multiple subsequent points had $|Q_{\text{north}} - Q_{\text{south}}| > 2\sigma$) immediately after said point, one can argue that the extent of the spherical cap representing minimal galactic influence is simply $80° - R_p$, for E_3 photons constrained to galactic latitudes of $80°$ or higher. Doing this for each energy bin gives us the appropriate spherical caps which we can use to compute the flux of extragalactic photons. Since the area of a spherical cap is $4\pi(1 - \sin(\theta))$ for a sphere of radius 1, the flux is simply

$$\Phi(\theta, \phi) = \frac{\sum_{|R|>80°-R_p} N(\theta, \phi)}{4\pi(1 - \sin(\theta))}. \tag{3.4}$$

3.6 Computing the Galaxy-Corrected Monte-Carlo

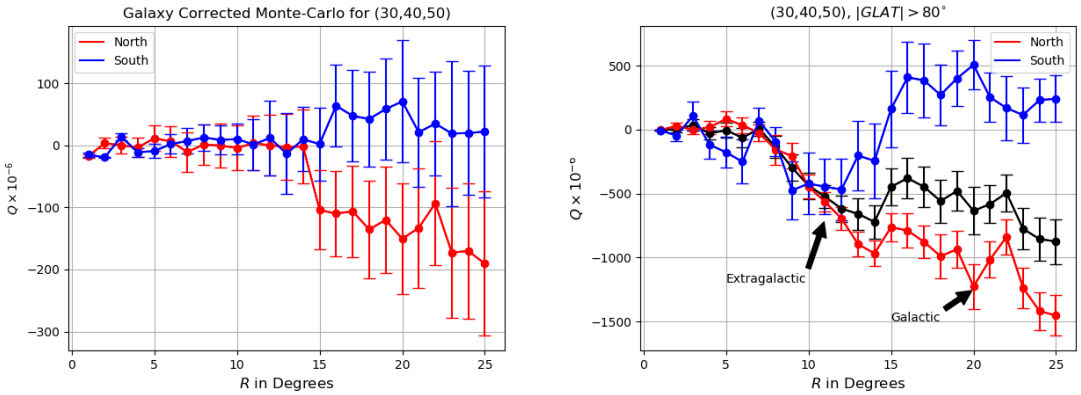

Figure 3.4: Comparison of Galaxy-Corrected Monte-Carlo vs observed data for $(30, 40, 50)$

Once we have determined both $p(\theta, \phi)$ and $\Phi(\theta, \phi)$, the Monte-Carlo can be computed as follows:

- For $|R| \geq 80° - R_p$ resample every point based on $p(\theta, \phi)$
- For $|R| < 80° - R_p$, during each realization, resample N points such that

$$N = \frac{\sum_{|R|<80°-R_p} N(\theta, \phi)}{4\pi(\sin(\theta))} \tag{3.5}$$

Figure 3.6 shows the $Q(R)$ curve obtained by generating and averaging over 10^4 realizations of the galaxy-corrected Monte-Carlo routine. In all, the simulation did spectacularly well given the fact that my estimate of R_p was measured purely through analysis of $Q(R)$. The predicted point of demarcation is slightly off, with the Monte-Carlo starting to deviate at $R \sim 14°$ and the observed data at $R \sim 12°$. In addition, the noise generated by randomly resampling points meant that the error-bars were fairly large and as a result, there were no points where Q_{north} and Q_{south} deviated by more than 2σ. Having said that, the Monte-Carlo clearly demonstrates the possibility of the hemispheric deviation being caused by interference from the galactic disk. Further analysis of the Monte-Carlo routine – and potentially a better method of benchmarking the extent of the galactic

sphere – might be a compelling direction for future work in uncovering the full effects of noise from the Milky Way.

Chapter 4

Discussion and Concluding Remarks

Analysis of signatures carried by extragalactic photons offer a very promising way of confirming the existence of large-scale extragalactic magnetic fields – and more generally in the observation of low-magnitude cosmological observables in the universe. A large amount of work done over the last decadesseem to suggest that the prescribed signature of a large-scale extragalactic field can be feasibly observed through analysis of photons from the Fermi LAT.(Tashiro et al., 2014; Kahniashvili and Vachaspati, 2006; Chen et al., 2015).

The work presented in this thesis adds to this body of knowledge by extending the existing analysis to a larger and more recent repository of data, as well as providing a potential answer to the problem of hemispheric deviation in the computed signal. Prior to this project, very little progress had been made in incorporating or accounting for galactic influence in Q and therefore, the Monte-Carlo routine suggested in Section 3.3 serves as a framework for future exploration of the topic.

In addition to this, the results in Chapter 2 demonstrate all of the predictions made in Section 1.3 – a very promising result that adds both to the validity of cascade photon analysis as a means of observing weak magnetic fields and to the existence of EGMF in general. Should the Monte-Carlo simulation presented in Chapter 3 be extended and used to explain away other anomalies that were not discussed as part of this document, such as discrepancies in peak placement ($(30, 40, 50)$ occurs after $(10, 40, 50)$) and show more definitive statistical significance in the deviation of hemispheric curves at large R, it would go a long way in enhancing the use of cascade photon analysis as a tool

for cosmological observation, and potentially settle the question of the existence of cosmic magnetic fields in general.

Bibliography

Aharonian, F., Akhperjanian, A. G., Bazer-Bachi, A. R., Beilicke, M., Benbow, W., Berge, D., Bernlhr, K., Boisson, C., Bolz, O., Borrel, V., Braun, I., Breitling, F., Brown, A. M., Chadwick, P. M., Chounet, L.-M., Cornils, R., Costamante, L., Degrange, B., Dickinson, H. J., Djannati-Ata, A., Drury, L. O., Dubus, G., Emmanoulopoulos, D., Espigat, P., Feinstein, F., Fontaine, G., Fuchs, Y., Funk, S., Gallant, Y. A., Giebels, B., Gillessen, S., Glicenstein, J. F., Goret, P., Hadjichristidis, C., Hauser, M., Heinzelmann, G., Henri, G., Hermann, G., Hinton, J. A., Hofmann, W., Holleran, M., Horns, D., Jacholkowska, A., de Jager, O. C., Khlifi, B., Komin, N., Konopelko, A., Latham, I. J., Gallou, R. L., Lemire, A., Lemoine-Goumard, M., Leroy, N., Lohse, T., Martin, J. M., Martineau-Huynh, O., Marcowith, A., Masterson, C., McComb, T. J. L., de Naurois, M., Nolan, S. J., Noutsos, A., Orford, K. J., Osborne, J. L., Ouchrif, M., Panter, M., Pelletier, G., Pita, S., Phlhofer, G., Punch, M., Raubenheimer, B. C., Raue, M., Raux, J., Rayner, S. M., Reimer, A., Reimer, O., Ripken, J., Rob, L., Rolland, L., Rowell, G., Sahakian, V., Saug, L., Schlenker, S., Schlickeiser, R., Schuster, C., Schwanke, U., Siewert, M., Sol, H., Spangler, D., Steenkamp, R., Stegmann, C., Tavernet, J.-P., Terrier, R., Thoret, C. G., Tluczykont, M., Vasileiadis, G., Venter, C., Vincent, P., Vlk, H. J., and Wagner, S. J. (2006). The h.e.s.s. survey of the inner galaxy in very high energy gamma rays. The Astrophysical Journal, 636(2):777.

Anderson, J., Burns, P. J., Milroy, D., Ruprecht, P., Hauser, T., and Siegel, H. J. (2017). Deploying rmacc summit: An hpc resource for the rocky mountain region. In Proceedings of PEARC17, New Orleans, LA, USA.

Bernet, M. L., Miniati, F., Lilly, S. J., Kronberg, P. P., and Dessauges-Zavadsky, M. (2008). Strong magnetic fields in normal galaxies at high redshift. Nature, 454:302 EP –.

Chen, W., Chowdhury, B. D., Ferrer, F., Tashiro, H., and Vachaspati, T. (2015). Intergalactic magnetic field spectra from diffuse gamma-rays. Monthly Notices of the Royal Astronomical Society, 450(4):3371–3380.

Clarke, T. E., Kronberg, P. P., and Bhringer, H. (2001). A new radio-x-ray probe of galaxy cluster magnetic fields. The Astrophysical Journal Letters, 547(2):L111.

Dolag, K., Borgani, S., Murante, G., and Springel, V. (2009). Substructures in hydrodynamical cluster simulations. Monthly Notices of the Royal Astronomical Society, 399(2):497–514.

Dolag, K., Kachelriess, M., Ostapchenko, S., and Toms, R. (2011). Lower limit on the strength and filling factor of extragalactic magnetic fields. The Astrophysical Journal Letters, 727(1):L4.

Donnert, J., Dolag, K., Lesch, H., and Mller, E. (2009). Cluster magnetic fields from galactic outflows. Monthly Notices of the Royal Astronomical Society, 392(3):1008–1021.

Kahniashvili, T. and Vachaspati, T. (2006). Detection of magnetic helicity. Phys. Rev. D, 73:063507.

Kronberg, P. P., Bernet, M. L., Miniati, F., Lilly, S. J., Short, M. B., and Higdon, D. M. (2008a). A global probe of cosmic magnetic fields to high redshifts. The Astrophysical Journal, 676(1):70.

Kronberg, P. P., Bernet, M. L., Miniati, F., Lilly, S. J., Short, M. B., and Higdon, D. M. (2008b). A global probe of cosmic magnetic fields to high redshifts. The Astrophysical Journal, 676(1):70.

McMillan, P. J. (2017). The mass distribution and gravitational potential of the milky way. Monthly Notices of the Royal Astronomical Society, 465(1):76–94.

Neronov, A. and Semikoz, D. V. (2009). Sensitivity of γ-ray telescopes for detection of magnetic fields in the intergalactic medium. Phys. Rev. D, 80:123012.

Porter, T. A., Jhannesson, G., and Moskalenko, I. V. (2017). High-energy gamma rays from the milky way: Three-dimensional spatial models for the cosmic-ray and radiation field densities in the interstellar medium. The Astrophysical Journal, 846(1):67.

Ryu, D., Kang, H., Cho, J., and Das, S. (2008). Turbulence and magnetic fields in the large-scale structure of the universe. Science, 320(5878):909–912.

Tashiro, H., Chen, W., Ferrer, F., and Vachaspati, T. (2014). Search for cp violating signature of intergalactic magnetic helicity in the gamma-ray sky. Monthly Notices of the Royal Astronomical Society: Letters, 445(1):L41–L45.

Tashiro, H. and Vachaspati, T. (2013). Cosmological magnetic field correlators from blazar induced cascade. Phys. Rev. D, 87:123527.

Tashiro, H. and Vachaspati, T. (2015). Parity-odd correlators of diffuse gamma-rays and intergalactic magnetic fields. Monthly Notices of the Royal Astronomical Society, 448(1):299–306.

Vachaspati, T. (2001). Estimate of the primordial magnetic field helicity. Phys. Rev. Lett., 87:251302.

Vachaspati, T. and Vilenkin, A. (1991). Large-scale structure from wiggly cosmic strings. Phys. Rev. Lett., 67:1057–1061.